Platinum group mineral (PGM) and Fe–Ni–As–S minerals in the Sartohay chromitite, Xinjiang (NW China): Implications for the mobility of Os, Ir, Sb, and As during hydrothermal processes

Yongfeng Zhu [a,*], Juanjuan Tan [a,b], Tian Qiu [a]

[a] The Key Laboratory of Orogenic Belts and Crustal Evolution, School of Earth and Space Sciences, Peking University, Beijing 100871, China
[b] Wuhan Center of Geological Survey, Wuhan 430223, China

ABSTRACT

The Sartohay chromitite deposit, hosted in the Sartohay ophiolite mélange in western Junggar (Xinjiang province, NW China), contains irarsite, breithauptite, and Fe–Ni–As–S minerals. Petrographic observations indicate that the chrome-spinel was firstly altered to Fe-rich chromite at low-temperature with relatively lower Fe^{3+}/Fe^{2+} ratios (0.14–0.34), and such Fe-rich chromite was altered to magnetite in a relatively oxidizing environment. Afterwards, irarsite, breithauptite, and Fe–Ni–As–S minerals formed during hydrothermal processes. A systematic change from magnetite–pentlandite, pentlandite–heazlewoodite–maucherite, millerite–breithauptite, to millerite–godlevskite–irarsite-dominated assemblage in the Sartohay chromitites suggests a complex evolutionary path in the $P–T–fS_2–fO_2$ space. Enrichments of Os, Ir, Sb, and As in disseminated irarsite, breithauptite, and Fe–Ni–As–S minerals reflect the mobility of Os, Ir, Sb, and As during low-temperature hydrothermal processes overprinting the chromitites in the Sartohay ophiolitic mélange.

© 2015 Elsevier B.V. All rights reserved.

1. Introduction

The association of chromite, sulfide, and platinum group mineral (PGM) is well-known and has been studied for decades (Prichard et al., 2001; Auge et al., 2005; Kapsiotis et al., 2011; Foustoukos et al., 2015). Podiform chromitites, occurring in the mantle sections of ophiolites, are mined for chromium. Base metal minerals commonly occur as accessory minerals in the inter-cumulus silicate matrix of chromitites, and platinum group elements (PGE: Os, Ir, Ru, Rh, Pt, Pd) may be concentrated in some minerals (Junge et al., 2015). Pt, Pd, and Rh-enriched podiform chromitites are less common than those enriched in Ir, Ru, and Os (collectively known as IPGE). Chromite (or chrome-spinel) has been proposed as an effective collector for IPGE (Finnigan et al., 2008).

Chromitite is generally considered to be a magmatic rock, or the product of melt/rock reaction at high temperature (e.g., Grieco et al., 2007; Robinson et al., 2015). In contrast, the origin of the sulfides in chromitites is unclear. Inclusions of metallic alloys and sulfides occur in many podiform chromitites (Uysal et al., 2009), indicating a mantle source and a relationship between sulfur and PGEs. However, the chromite and PGM generally are not cogenetic in ophiolite (Brough et al.,

2015). Although the primary PGE-bearing arsenides and sulfarsenides have been found in ophiolitic chromitites (Kapsiotis et al., 2011), most researchers suggested that the Co–Ni arsenide ores were formed by magmatic fluids interacting with serpentinites (Ahmed et al., 2009; Brough et al., 2015). Because late-stage metamorphic or hydrothermal events commonly overprint podiform chromitites, it is difficult to determine whether the base metal sulfides, are magmatic or hydrothermal in origin. In this study, we describe the breithauptite, PGMs, and Fe–Ni–As–S minerals newly found in the Sartohay chromitite, with special emphasis on the intergrowth of maucherite, pentlandite, heazlewoodite, millerite, breithauptite, irarsite and its geological significance.

2. Geological background

The Sartohay podiform chromitite deposit in western Junggar of Xinjiang (NW China) is hosted in the Sartohay ophiolitic mélange (Fig. 1). This ophiolite mélange is a major component of the Darbut (also known as Dalabute)–Sartohay ophiolite belt. On its south side is the Baijiantan–Baikouquan ophiolitic mélanges, which connect with the Tangbale ophiolitic mélanges to southwest and constitute the Tangbale–Baijiantan–Baikouquan (TBB) ophiolite belt (Zhu et al., 2015, Fig. 1c). The Darbut–Sartohay ophiolite belt was dated as early Devonian based on radiolarian fossils in chert (Feng, 1986). However, zircons separated from metagabbro in the Darbut ophiolite mélange were dated at 426 Ma (Chen and Zhu, 2011). There are two types of
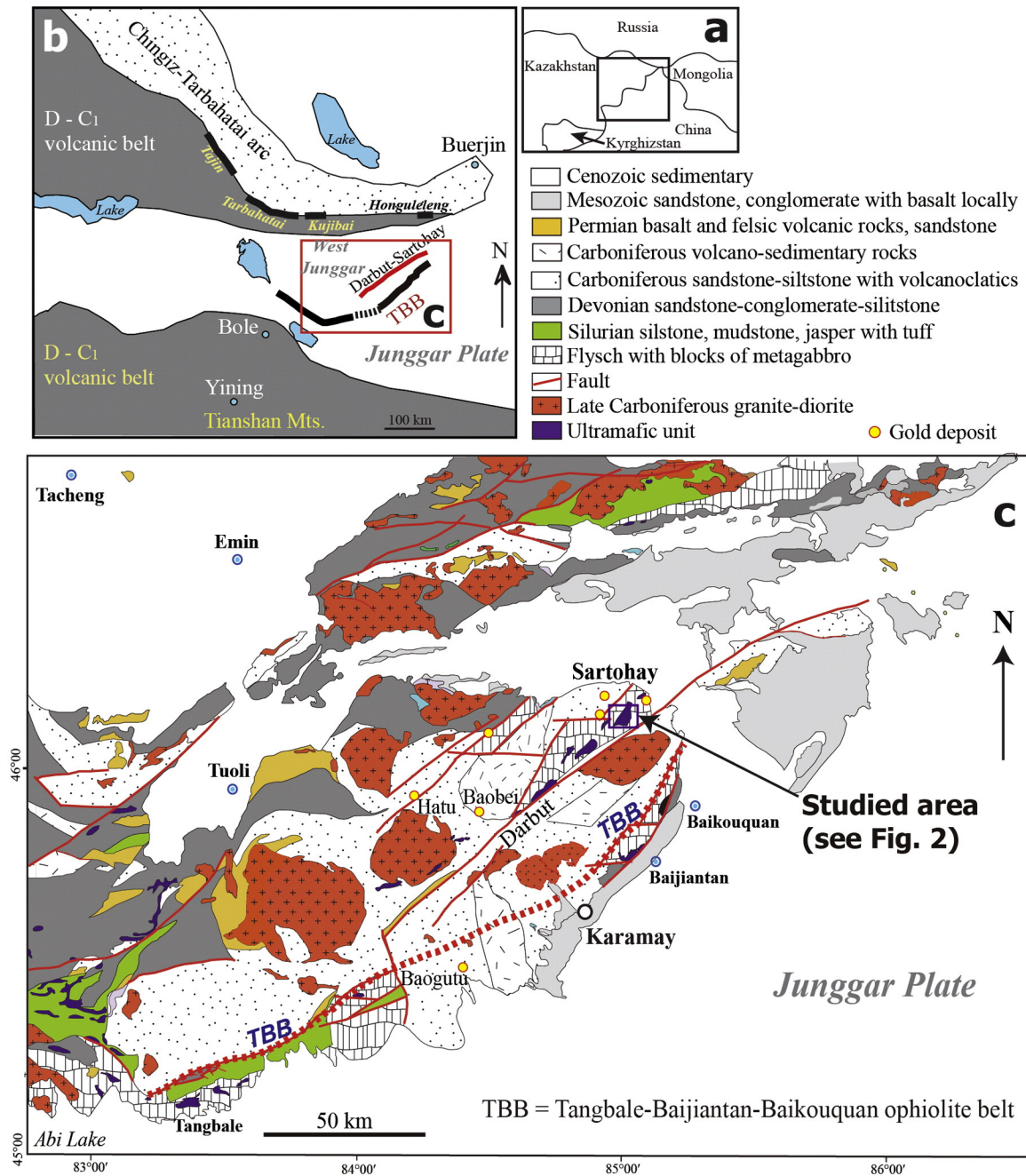
Fig. 1. Simplified geological map of western Junggar showing the Tangbale–Baijiantan–Baikouquan ophiolite belt (TBB) and Darbut–Sartohay ophiolitic mélange (after Zhu et al., 2013).

gabbros in the Sartohay region: one is gabbro-diorite pluton, which intruded the flysch covering on ophiolitic mélanges; another is metagabbro which only occurs in serpentinite as lenses and was subject to metamorphism, hence the prefix meta (Zhu et al., 2013). The gabbro-diorite pluton formed during late Carboniferous period with U–Pb ages of 315–305 Ma (Liu et al., 2008; Zhu et al., 2013), while zircons separated from metagabbro lenses generally give Silurian to early Devonian U–Pb ages (434–391 Ma, Gu et al., 2009; Zhu et al., 2013). Zircons separated from metagabbro sample from the Sartohay ophiolitic mélange was dated by SIMS (Zhu et al., in preparation). There are three types of zircons: (a) zircons with U–Pb ages of 2472–2333 Ma could be interpreted as detrital origin derived from recycled old continental crust; (b) zircons with U–Pb ages of 438–432 Ma with weak oscillatory zoning interpreted as having crystallized from mafic magma, and their U–Pb ages should represent the formation time of gabbro crystallization in Sartohay ophiolitic mélange; (c) hydrothermal

zircons with U–Pb ages of 310–288 Ma probably formed during the hydrothermal and/or metamorphic period overprinting the Sartohay chromitites, similar to the hydrothermal zircons formed during mylonitization of granite (Zhu, 2011).

Flysch, mainly consisting of chert and siltstone-tuff, overlies the ophiolitic mélange. Rock units including basalt, metagabbro, serpentinite and flysch are strongly deformed and showing closely spaced cleavage. The serpentinite with peridotite lenses were covered by the undeformed Devonian sandstone and conglomerate unconformably. Flysch is in contact with horizontal strata of the Early Carboniferous volcanoclastics whereas peridotite and serpentinite units are in tectonic contact with Devonian-Carboniferous volcano-sedimentary rocks. These sedimentary rocks host several gold deposits (see Fig. 1c for locations). The ultramafic units in the northern part of Sartohay ophiolitic mélange were transformed to talc listwaenite along a shear zone, hosting several gold deposits (Qiu and Zhu, 2015).

A geological profile across the Sartohay ophiolitic mélange shows the details of rock units (Fig. 2a–b). Metagabbro lenses with sizes ranging from several ten centimeters to meters generally occur in serpentinite, and such serpentinite-metagabbro units are in fault contact with basalt-jasper interlayers. Serpentinite and peridotite with chromitite lenses occasionally occur at the stratigraphic bottom of the Sartohay ophiolitic mélange (Fig. 2c). The Sartohay chromitite deposit has several clusters of ore bodies. The major mining area named as No. 24 Group ores is shown in Fig. 2d with sample location.

3. Analytical methods

An energy-dispersive system (EDS) installed in JEOL JXA-8100 at Peking University was used to initially identify minerals (Table 1) and to carry out X-ray mapping to determine textures and zoning of the PGMs. Operating conditions were set at 15 kV and 5 nA using a beam focused close to 0 μm in order to get a clear image. Dwell time for each point was 40 ms. The number of pixels in each image was set to 600 with a pixel size of 0.01 μm. Mineral compositions were obtained using a JXA-8100 wavelength dispersive electron microprobe. An acceleration voltage of 20 kV and a beam current of 10 nA were used for all analyses. The beam diameter was set at about 1 μm, and counting times of 20 s were used for both peak and background. Synthetic and natural minerals, glasses and pure oxides were used as standards. The ZAF correction method was used for standardization. The detection limits of elements in PGMs and Fe–Ni–As–S minerals are 0.01 wt.% for As, Co, Te, Os, and Ir; 0.02% for Fe, Ni, S, Sb, Ru, and Rh.

4. Ore deposit and mineralogy

4.1. Sartohay chromitite

As a typical ophiolite-associated chromitite, the Sartohay deposit occurs as pods, lenses and bands (Figs. 2d and 3a,b). Most ores are massive or disseminated with >80 vol.% chrome-spinels, but nodular varieties are also present. The ore bodies are concordant with banding in host harzburgite and are surrounded by serpentinized dunite envelope. Chloritite halos, up to centimeter thick, commonly separate the chromitite from the surrounding serpentinite (Fig. 3b). Chromitite is generally composed of chrome-spinels with cumulate texture (Fig. 3c).

Table 1
Identified opaque minerals in the Sartohay chromitite and chromitite-bearing serpentinite (in order of abundance).

Mineral	Chemical formula	Abbreviations used in this paper
Chrome-spinel	Cr_2AlO_4	Cr-spl
Fe-rich chromite	$(Cr\ Fe)_2AlO_4$	Chr
Magnetite	Fe_3O_4	Mt
Pentlandite	$(Fe\ Ni)_9S_8$	Pn
Heazlewoodite	Ni_3S_2	Hz
Millerite	NiS	Ml
Maucherite	$Ni_{11}As_8$	Mr
Breithauptite	$NiSb$	Brp
Godlevskite	Ni_9S_8	Gl
Chalcocite	Cu_2S	
Chalcopyrite	$CuFeS_2$	
Niccolite	$NiAs$	
Polydymite	Ni_3S_4	
Irarsite	$IrAsS$	PGM

Interstitial silicates (olivine, pyroxene) in chromitite have been altered to chlorite, and locally cut by veinlets of calcite and brucite. Small, round to elongated or distorted grains of magnetite are common in chloritite (Fig. 3d).

Chrome-spinel grains exhibit variable degrees of alteration on their margins and along fractures. Fresh chrome-spinel grains are translucent and reddish-brown to orange in polarized light (Fig. 3c), whereas altered grains are opaque (Fig. 3e). More than half chrome-spinel grains have well-developed altered rims, and those closer to the chloritite envelopes have undergone more extensive alteration (Fig. 3b). The altered parts usually form an irregular zone/rim around the fresh core, showing greater reflectivity (Fig. 3f). The altered parts are Fe-rich chromite, which was further replaced by magnetite (Fig. 4).

Representative compositions of the chrome-spinel cores and their Fe-rich chromite rims are listed in Table 2. The observed increase of Cr contents and corresponding drop of Al and Mg contents are consistent with the different reflectivity of cores (chrome-spinel) and rims (Fe-rich chromite). The chrome-spinels cluster in a restricted range in the middle between Cr and Al end-members in triangular plot (Fig. 5a), whereas the altered rims scatter in the area close to the Cr end-member. Spinels in the Darbut ophiolitic mélange and spinels in the Kujibai ophiolitic mélange are also shown for comparison in Fig. 5a.
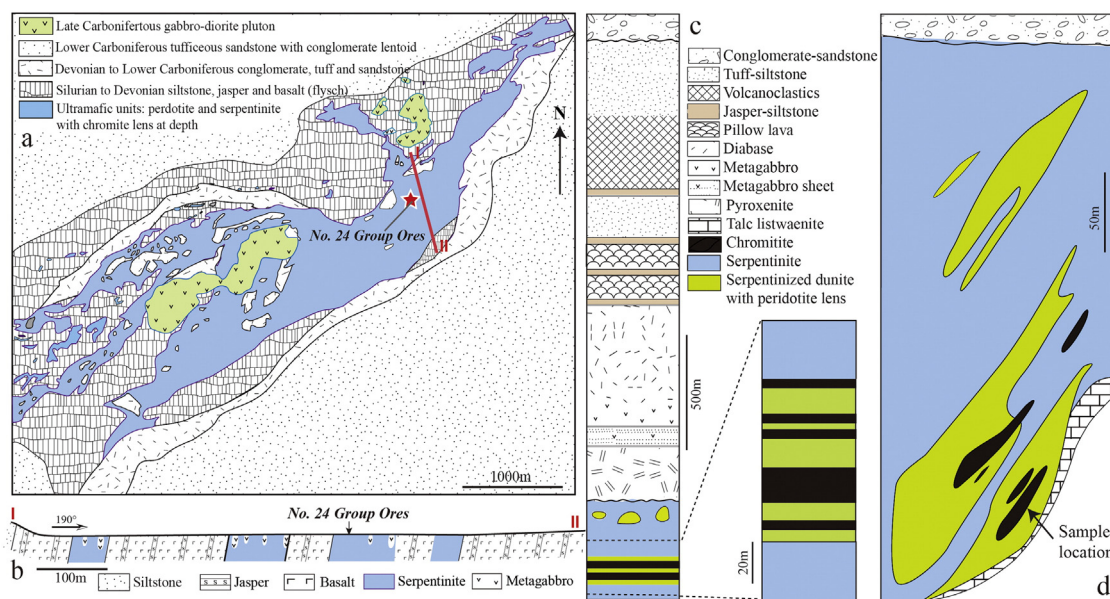
Fig. 2. (a) Geological map showing the Sartohay ophiolite mélange; (b) Geological profile of the ophiolite mélange passing through the No. 24 Group ores; (c) Compiled geological profile showing rock units of the Sartohay ophiolite mélange with enlarged section showing the lower part containing chromitite lenses; (d) Section showing the No. 24 Group ores in Sartohay (based on data from the local mining company).
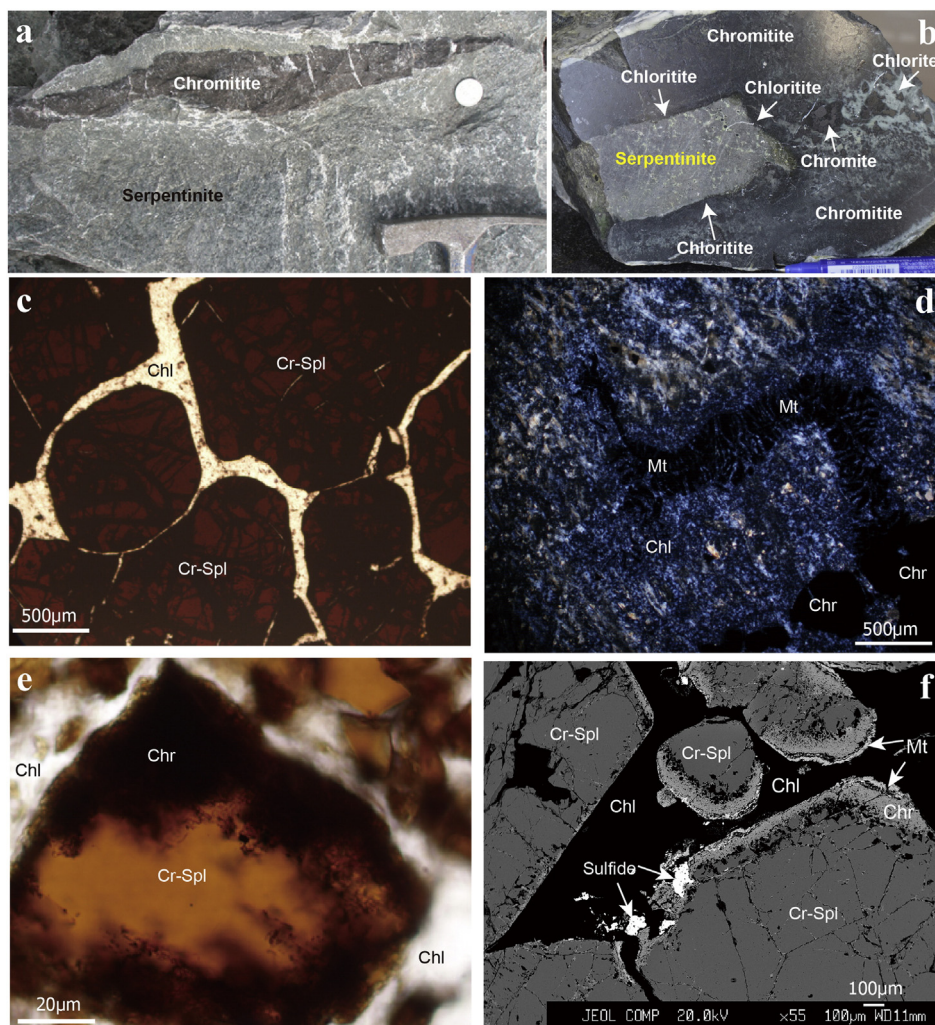
Fig. 3. (a) Photo showing one small chromitite lens in serpentinite; (b) A thin chlorite film occurring in between chromitite and serpentinite; (c) Photomicrograph of chrome-spinels with chlorite (Chl) in their boundary, plane polarized light; (d) Photomicrograph showing magnetite grains in chloritite, cross-polarized light; (e) Chrome-spinel was altered to Fe-rich chromite on rim, plane polarized light; (f) Sulfides distributed along an altered chrome-spinel rim (e.g., Fe-rich chromite + magnetite), back-scattered electron (BSE). For mineral abbreviations see Table 1.

For example, spinels in the Darbut serpentinite plot almost in the same area as chrome-spinels in the Sartohay, while spinels in the Kujibai serpentinite are highly variable. The contents of magnetite end-member in the altered rims are higher and highly variable comparing with that in the chrome-spinel cores (Fig. 5b). The $Cr^{\#}$ values and Fe^{3+}/Fe^{2+} ratios are relatively uniform in the chrome-spinel cores (0.48–0.53 and 0.21–0.34, respectively), whereas these values are highly variable for the Fe-rich chromite rims (0.69–0.82 and 0.14–0.32, respectively, Table 2).

4.2. Fe–Ni–As–S minerals

The base metal sulfides and arsenides are randomly distributed in the Sartohay chromitites and chloritites. In the chromitites, sulfides and arsenides account for less than 1 vol.%, whereas these minerals range up to 5 vol.% in the chloritite. The observed mineral phases include pentlandite, heazlewoodite, millerite, maucherite, breithauptite, godlevskite, chalcocite, chalcopyrite, niccolite, polydymite, and irarsite (Table 1). All these minerals are secondary in origin comparing with the chrome-spinels in the Sartohay chromitites. For example, most breithauptite and millerite grains occurring in magnetite and chlorite matrix, which generally surround the Fe-rich chromite rim of the chrome-spinel core (Fig. 4). Representative compositions of selected

pentlandite, millerite, heazlewoodite, and maucherite are listed in Tables 3, 4, 5, and 6, respectively.

Compared to the arsenides (maucherite, niccolite), sulfides are relatively common in the studied samples. Pentlandite, heazlewoodite and millerite occur along fractures in Fe-rich chromite and magnetite or as intercumulus phases in chromitites (Fig. 6a,b). The sulfide grains generally range from several μm to 100 μm across. Pentlandite grains in the chromitites are highly fractured and exhibit variable reflectivity, corresponding to large variations in Ni (43.2–54.1%) and Fe contents (12.1–22.9%, Table 3). In contrast, the pentlandite in chloritite is relatively homogeneous in composition. The As and Te contents in pentlandite grains are below 1 wt.% and the Sb is below detection limit in most cases. Pentlandite generally was replaced by heazlewoodite (Fig. 6c), and by millerite–heazlewoodite assemblage (Fig. 6d). Millerite also replaced heazlewoodite as shown in Fig. 6d. Most millerite grains fit the ideal stoichiometric formula with an atomic ratio of Ni:S = 1:1 (Table 4). Heazlewoodite has a similar composition in both chromitite and chloritite with trace amounts of Fe (up to 0.93%) and Te (0.69%–0.96%, Table 5).

Maucherite occurs in two different forms: (1) maucherite grains coexisting with heazlewoodite, and/or replacing millerite (Fig. 7a) and pentlandite (Fig. 6c); and (2) maucherite droplets (up to 10 μm) with a worm-like texture occurring within pentlandite and heazlewoodite (Fig. 7b–c). Such worm-like droplets of maucherite are frequently
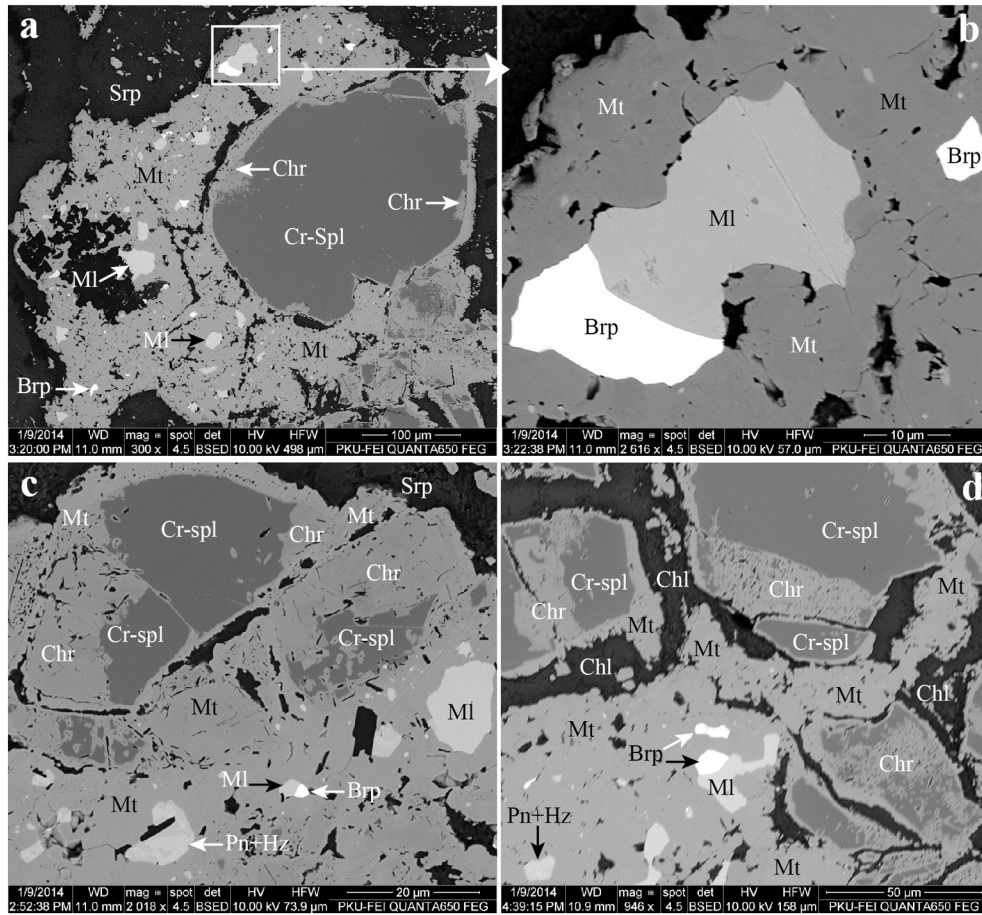
Fig. 4. BSE images showing millerite–breithauptite and pentlandite–heazlewoodite assemblage in magnetite matrix surrounding the altered chrome-spinel in Sartohay. Chrome-spinel was firstly altered to chromite, and further altered to magnetite. For mineral abbreviations see Table 1.

observed both in chloritite and chromitite. Maucherite from chromitite and chloritite is generally similar in composition (Table 6).

Mineral compositions of these sulfides and arsenides are shown in Fig. 8 for comparison. Maucherite and heazlewoodite contain relatively higher Ni contents than millerite and pentlandite (Fig. 8a), and the visa versa for Fe contents (Fig. 8b). Maucherite with higher and highly variable Sb contents differs from heazlewoodite and pentlandite (Fig. 8c). The Co contents in pentlandite are highly variable (up to >4 wt.%), while other minerals contain only trace amounts of Co (Fig. 8d).

4.3. PGM in Sartohay chromitite

Sparse, minute grains of PGMs, generally associated with heazlewoodite, millerite, and godlevskite (Figs. 9, 10a,b), fill fractures or occur on edges of the Fe-rich chromite in the Sartohay chromitites. X-ray mapping shows that S and Ni are homogenously distributed in millerite grains (Fig. 10c and e, respectively), and that neither As nor Ir is present (Figs. 10d and f, respectively). The X-ray mapping also shows that the PGM consists mainly of As, Ir, and S, and is most probably irarsite (IrAsS) considering the S content of irarsite is lower than that in millerite.

All the studied PGM grains are sulfides or sulfarsenides based on EDS observations and only several PGM grains were conducted EPMA analysis (Table 7). Most PGM grains are less than 2 μm across, making it difficult to obtain accurate compositions. The EPMA analyses for such small PGM grains are easy to be contaminated by neighboring minerals and thus their compositions only could be used for reference. Some PGM grains contain detectable amounts of Fe, Ni, As, and Sb,

while neither Pt nor Pd has been detected. The compositions listed in Table 7 could represent two mineral phases: irarsite and other PGMs, which are quite different in composition as shown in Fig. 8e–f.

5. Discussion

5.1. Origin of podiform chromitite and refining process of chrome-spinel

Podiform chromite deposits are defined as irregular, but fundamentally lenticular, chromite-rich bodies that occur within mantle peridotites of ophiolite complexes. Chromitites have large variations in their major oxide compositions, belonging to either high-Cr or high-Al varieties. Studies on chromite ores worldwide show the complexity of relationships among lithologies that reflects the subtlety of genetic events and of chromite ore occurrence. The chromite ore genetic process is related to a supra-subduction geodynamic setting where partial melting processes were overprinted by metasomatic events (Zhou et al., 2014; McGowan et al., 2015). These authors suggested that the tearing and breakoff of the subducted slab create a slab window through which the underlying asthenosphere rises and melts to generate Cr-rich mafic magmas. As a result of slab contamination during upward-migrating, these magmas become more siliceous, more oxidized and more hydrous, rapidly triggering chromite crystallization.

Various combinations of zircon, quartz, apatite, rutile, garnet, kyanite, and some unusual minerals including coesite and diamond have been recovered from podiform chromitites of different ophiolites (Yang et al., 2007, 2015; Robinson et al., 2015). However, we did not find any diamond or other ultrahigh-pressure minerals in our samples under both optical and electronic microscope for thousands of spinel-

Table 2
Representative compositions of chrome-spinels (Sp1–Sp15) and Fe-rich chromites (Chr1–Chr7) from the Sartohay chromitite.

wt.%	Sp1	Sp2	Sp3	Sp4	Sp5	Sp6	Sp7	Sp8	Sp9	Sp10	Sp11	Sp12	Sp13	Sp14	Sp15	Chr1	Chr2	Chr3	Chr4	Chr5	Chr6	Chr7
SiO$_2$	0.03	bdl	bdl	bdl	0.02	bdl	bdl	0.11	0.04	0.24	0.05	0.03	0.02	0.03	0.03	1.06	0.82	0.43	0.05	0.11	0.23	0.10
TiO$_2$	0.28	0.24	0.33	0.33	0.03	0.29	0.35	0.06	0.11	0.06	0.05	0.09	0.05	0.02	0.05	0.42	0.36	0.28	0.48	0.53	0.51	0.47
Al$_2$O$_3$	27.94	28.46	28.25	28.31	28.46	28.17	28.39	27.49	28.11	27.92	28.04	25.48	25.58	24.78	25.04	14.19	14.21	13.00	13.01	12.63	12.6	8.22
MgO	15.68	15.61	15.58	15.71	15.57	15.92	15.92	15.79	15.22	15.21	15.18	12.11	12.37	11.90	11.60	9.83	9.31	8.99	8.99	8.94	9.05	7.35
MnO	0.23	0.19	0.26	0.22	0.26	0.24	0.23	0.17	0.22	0.18	0.21	0.24	0.34	0.26	0.26	0.58	0.54	0.64	0.53	0.58	0.54	0.65
FeO	15.66	15.42	15.44	15.13	15.30	15.20	15.16	15.64	15.78	15.66	15.79	21.35	21.41	21.95	21.88	25.63	24.29	24.88	22.93	22.56	21.77	24.29
Cr$_2$O$_3$	39.14	39.73	39.78	39.48	39.48	39.07	39.49	40.49	40.07	40.39	40.21	40.63	40.88	41.78	40.31	46.95	48.01	48.77	51.29	53.20	53.21	57.51
NiO	0.15	0.12	0.13	0.21	0.17	0.12	0.19	0.32	0.28	0.22	0.28	0.16	0.08	0.04	0.08	0.08	0.07	0.12	0.10	0.13	0.06	0.05
Total	99.11	99.77	99.77	99.39	99.56	99.01	99.73	100.07	99.83	99.88	99.81	100.09	100.73	100.76	99.25	98.74	97.61	97.11	97.38	98.68	97.97	98.64
O = 4																						
Si	0.001	0.000	0.000	0.000	0.001	0.000	0.000	0.003	0.001	0.007	0.001	0.001	0.001	0.001	0.001	0.034	0.028	0.015	0.002	0.004	0.008	0.003
Ti	0.000	0.000	0.000	0.000	0.000	0.000	0.000	0.000	0.000	0.000	0.000	0.000	0.000	0.000	0.000	0.000	0.000	0.000	0.000	0.000	0.000	0.000
Al	0.980	0.992	0.986	0.990	0.993	0.987	0.987	0.955	0.981	0.974	0.979	0.914	0.911	0.888	0.910	0.548	0.556	0.515	0.517	0.496	0.499	0.334
Mg	0.696	0.688	0.688	0.694	0.688	0.705	0.701	0.694	0.672	0.671	0.670	0.550	0.557	0.540	0.533	0.480	0.461	0.450	0.451	0.444	0.453	0.377
Mn	0.006	0.005	0.007	0.006	0.007	0.006	0.006	0.004	0.006	0.005	0.005	0.006	0.009	0.007	0.007	0.016	0.015	0.019	0.015	0.016	0.015	0.019
Fe^{3+}	0.098	0.080	0.083	0.085	0.080	0.095	0.091	0.095	0.080	0.067	0.078	0.106	0.110	0.106	0.106	0.167	0.127	0.160	0.114	0.093	0.074	0.094
Fe^{2+}	0.292	0.301	0.299	0.290	0.299	0.283	0.284	0.290	0.310	0.320	0.313	0.438	0.431	0.452	0.457	0.535	0.547	0.539	0.531	0.537	0.537	0.604
Cr	0.920	0.928	0.931	0.925	0.925	0.918	0.922	0.943	0.937	0.945	0.941	0.978	0.977	1.004	0.982	1.216	1.261	1.296	1.365	1.403	1.412	1.566
Ni	0.007	0.006	0.006	0.010	0.008	0.006	0.009	0.015	0.013	0.011	0.013	0.008	0.004	0.002	0.004	0.004	0.004	0.007	0.005	0.007	0.003	0.003
Cr#	0.484	0.484	0.486	0.483	0.482	0.482	0.483	0.497	0.489	0.493	0.490	0.517	0.518	0.531	0.519	0.689	0.694	0.716	0.726	0.739	0.739	0.824
Fe^{3+}/Fe^{2+}	0.243	0.255	0.234	0.232	0.328	0.259	0.209	0.249	0.334	0.266	0.278	0.293	0.269	0.335	0.319	0.312	0.233	0.297	0.215	0.173	0.137	0.156
Spinel, mol%	49.04	49.59	49.29	49.49	49.70	49.34	49.37	47.90	49.08	49.04	48.99	45.74	45.59	44.44	45.54	28.38	28.61	26.12	25.88	24.91	25.13	16.75
Chromite, mol%	46.07	46.41	46.56	46.26	46.28	45.92	46.10	47.31	46.90	47.59	47.11	48.95	48.90	50.26	49.14	62.98	64.84	65.75	68.39	70.43	71.16	78.51
Magnetite, mol%	4.89	4.00	4.15	4.25	4.02	4.74	4.53	4.78	4.03	3.38	3.90	5.32	5.51	5.30	5.32	8.64	6.55	8.13	5.73	4.66	3.72	4.74

Cr# = Cr / (Cr + Al); bdl = below detection limit.
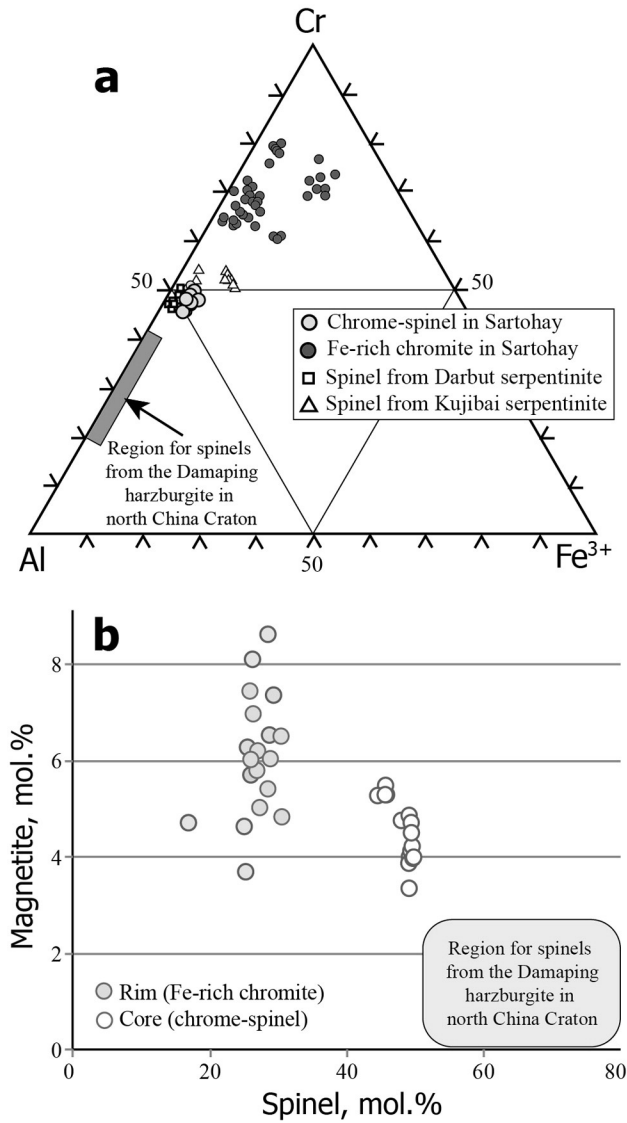
Fig. 5. (a) Triangular compositional plot for spinel-chromites from the Sartohay chromitite and adjacent areas; (b) Plot of spinel end-member vs. magnetite end-member showing the large difference between chrome-spinel cores and Fe-rich chromite rims. The Damaping spinels from harzburgite in north China Craton (Zhu, 2008) are shown for comparison. Spinels from the Kujibai serpentinite are based on Zhu and Xu (2006) and spinels from the Darbut serpentinite are based on Chen and Zhu (2008).

chromite and zircon grains. This might means that there is a multi-stage process of the chromitite as suggested by some researchers (Gervilla et al., 2012; Derbyshire et al., 2013; Zhou et al., 2014). We also note that those who reported ultrahigh-pressure minerals in chromitite do not mention any sulfides and arsenides. It is quite possible that the chromitite samples with high contents of sulfides and arsenides have undergone strong hydrothermal alteration. The primary ultrahigh-pressure minerals might have been completely erased during the hydrothermal processes if ever formed in the Sartohay chromitite. However, we found abundant quartz and apatite in zircons separated from the Sartohay ophiolitic mélange. For example, zircons separated from metagabbro in the Sartohay ophiolitic mélange have complex U–Pb age patterns ranging from 2572 Ma to 288 Ma (Zhu et al., in preparation). Zircons with U–Pb ages of 2472–2333 Ma usually contain inclusions such as quartz and apatite indicating their origin of recycled old continental crust, while zircons with U–Pb ages of 438–432 Ma do not contain any inclusions. These Silurian zircons probably represent the formation time of gabbro crystallization in the Sartohay ophiolitic mélange. These U–Pb ages may approximate the age of chromitites in the Sartohay region.

Both spinel and chromite are relatively resistant to fluid-driven alteration and weathering relative to associated silicate minerals and thus may preserve original magmatic features. However, post-magmatic alteration of chrome-spinel can produce Fe-rich chromite (Mellini et al., 2005; Chen and Zhu, 2008; Gervilla et al., 2012), as shown in the Sartohay ophiolitic mélange where the altered Fe-rich chromites are enriched in FeO and Cr_2O_3 (Zhou et al., 2014). As a consequence, Cr#s of the altered Fe-rich chromites can be significantly increased to values much higher than the primary grains and even higher than the high-Cr group of metallurgical chromitites. In mélange environments, intense metamorphism above 300 °C leads to major changes in chrome-spinel chemistry and to the growth of secondary phases such as Fe-rich chromite and chlorite. Three different spinels have been distinguished within serpentinites (Mellini et al., 2005): magmatic spinel, hydrothermally altered spinel, and metamorphic syn-serpentinization magnetite. After the main serpentinization, spinel was progressively replaced by Fe-rich chromite rim by a dissolution–recrystallization process. This is very similar to the chrome-spinel core, Fe-rich chromite rim, and magnetite surrounding the Fe-rich chromite (Fig. 4) in the Sartohay chromitites (see Section 4.1 for details).

The Fe-rich chromite rims surrounding chrome-spinels probably formed during serpentinization of ultramafic rocks, which generally occurred at highly reducing conditions and low-temperatures (200–400 °C; Evans, 2004; Merlini et al., 2009). These authors have recognized a low-temperature metasomatic stage characterized by the replacement of olivine with serpentine, followed by a moderate-

Table 3
Representative compositions of pentlandite in chromitite and in chloritite from Sartohay.

	R	R	R	R	R	R	R	R	R	L	L	L	L	L	L	L	L	L
Fe	18.06	12.25	12.11	22.90	14.57	12.17	12.22	16.12	14.02	24.01	23.54	22.32	21.69	22.50	23.91	23.11	22.92	21.91
As	0.06	0.08	0.10	0.04	0.20	0.11	0.12	0.04	0.23	0.33	0.07	0.28	0.14	0.18	0.31	0.12	0.28	0.24
S	33.65	33.51	32.95	32.62	30.31	33.42	33.31	33.61	31.24	32.06	32.66	32.55	32.56	32.53	32.41	32.94	32.41	32.68
Co	0.48	0.15	0.26	0.25	1.69	0.13	0.21	0.27	1.69	3.47	5.33	4.83	4.79	5.98	3.79	5.13	4.81	4.74
Sb	bdl	bdl	bdl	bdl	bdl	0.01	0.01	0.02	0.01	bdl	bdl	bdl	bdl	bdl	0.02	0.01	0.02	0.01
Ni	47.45	54.11	53.27	43.23	52.11	53.52	53.43	48.97	52.01	39.79	38.35	39.29	39.35	37.66	38.84	38.23	39.01	39.47
Te	0.53	0.60	0.58	0.56	0.70	0.61	0.67	0.79	0.77	0.53	0.46	0.54	0.52	0.48	0.53	0.39	0.53	0.67
Total	100.23	100.70	99.27	99.60	99.58	99.97	99.97	99.82	99.97	100.19	100.41	99.81	99.05	99.33	99.81	99.93	99.98	99.72
Atom																		
Fe	0.147	0.100	0.100	0.189	0.122	0.100	0.100	0.130	0.117	0.198	0.193	0.184	0.180	0.186	0.197	0.189	0.189	0.181
As	0.000	0.001	0.001	0.000	0.001	0.001	0.001	0.000	0.001	0.002	0.000	0.002	0.001	0.001	0.002	0.001	0.002	0.001
S	0.478	0.476	0.475	0.468	0.444	0.478	0.477	0.480	0.453	0.460	0.465	0.467	0.470	0.468	0.465	0.470	0.465	0.469
Co	0.004	0.001	0.002	0.002	0.013	0.001	0.002	0.002	0.013	0.027	0.041	0.038	0.038	0.047	0.030	0.040	0.038	0.037
Sb	0.000	0.000	0.000	0.000	0.000	0.000	0.000	0.000	0.000	0.000	0.000	0.000	0.000	0.000	0.000	0.000	0.000	0.000
Ni	0.368	0.420	0.420	0.339	0.417	0.418	0.418	0.382	0.412	0.312	0.299	0.308	0.310	0.296	0.304	0.298	0.306	0.309
Te	0.002	0.002	0.002	0.002	0.003	0.002	0.002	0.003	0.003	0.019	0.002	0.002	0.002	0.002	0.002	0.001	0.002	0.002

R = pentlandite in chromitite; L = pentlandite in chloritite; bdl = below detection limit.

Table 4
Representative compositions of millerite in chromitite and in chloritite from Sartohay.

wt.%	R	R	R	R	R	R	R	R	R	R	L	L	L	L	L	L
Fe	1.13	2.75	0.87	1.14	1.05	0.77	1.63	0.21	1.41	1.12	0.11	0.37	2.66	1.17	2.02	1.29
As	bdl	0.05	0.13	0.31	0.24	0.32	0.22	0.18	0.22	0.14	0.16	0.17	0.20	0.14	0.15	0.25
S	33.66	34.20	32.33	32.54	34.41	35.01	33.16	35.01	33.71	34.21	34.54	35.27	32.47	34.08	34.32	34.21
Co	0.56	0.12	0.64	0.41	0.23	0.21	0.32	0.19	0.32	0.41	0.30	0.22	0.32	0.47	0.12	0.24
Sb	0.02	bdl	bdl	0.02	0.02	0.04	0.01	0.21	0.13	0.03	0.01	bdl	0.01	0.01	0.03	0.11
Ni	63.98	61.94	65.65	64.77	63.24	62.75	63.81	62.94	63.18	63.19	63.8	62.51	62.68	63.01	62.42	63.02
Te	0.75	0.73	0.75	0.79	0.67	0.79	0.77	0.91	0.74	0.82	0.83	0.79	0.79	0.72	0.79	0.67
Total	100.10	99.79	100.37	99.98	99.86	99.89	99.92	99.65	99.71	99.92	99.75	99.33	99.13	99.60	99.85	99.79
Atom																
Fe	0.009	0.023	0.007	0.009	0.009	0.006	1.003	0.002	1.002	0.009	0.001	0.003	2.002	0.010	1.007	1.006
As	0.000	0.000	0.001	0.002	0.001	0.002	0.001	0.001	0.001	0.001	0.001	0.001	0.001	0.001	0.001	0.002
S	0.482	0.489	0.467	0.471	0.491	0.499	0.478	0.500	0.485	0.490	0.494	0.504	0.473	0.489	0.491	0.490
Co	0.004	0.001	0.005	0.003	0.002	0.002	0.003	0.001	0.003	0.003	0.002	0.002	0.003	0.004	0.001	0.002
Sb	0.000	0.000	0.000	0.000	0.000	0.000	0.000	0.001	0.000	0.000	0.000	0.000	0.000	0.000	0.000	0.000
Ni	0.501	0.484	0.518	0.512	0.494	0.488	0.502	0.491	0.496	0.494	0.499	0.488	0.498	0.494	0.488	0.493
Te	0.003	0.003	0.003	0.003	0.002	0.003	0.003	0.003	0.003	0.003	0.003	0.003	0.003	0.003	0.003	0.002

R = millerite in chromitite; L = millerite in chloritite; bdl = below detection limit.

Table 5
Representative compositions of heazlewoodite in chromitite and in chloritite from Sartohay.

wt.%	R	R	R	R	R	R	R	L	L	L	L	L
Fe	0.20	0.06	bdl	0.09	0.54	0.62	0.93	0.58	0.36	0.94	0.64	0.16
As	0.05	bdl	bdl	0.11	0.12	0.12	0.13	0.13	0.10	0.01	0.04	0.02
S	26.71	26.28	26.54	26.04	26.11	26.08	26.05	26.36	26.48	26.50	26.11	26.28
Co	bdl	0.01	bdl	0.11	0.02	0.02	0.11	bdl	0.03	bdl	0.01	0.01
Sb	bdl	0.02	bdl	0.01	0.03	0.04	0.03	bdl	bdl	0.02	0.02	0.02
Ni	72.80	72.51	73.36	72.81	72.12	72.29	71.94	72.41	72.09	71.40	72.28	72.42
Te	0.89	0.91	0.96	0.69	0.84	0.81	0.78	0.89	0.78	0.77	0.87	0.91
0.00	100.65	99.79	100.86	99.86	99.78	99.98	99.97	100.37	99.84	99.64	99.97	99.82
Atom												
Fe	0.002	0.001	0.000	0.001	0.005	0.005	0.008	0.005	0.003	0.008	0.006	0.001
As	0.000	0.000	0.000	0.001	0.001	0.001	0.001	0.001	0.001	0.000	0.000	0.000
S	0.400	0.397	0.397	0.394	0.395	0.394	0.393	0.396	0.399	0.400	0.394	0.397
Co	0.000	0.000	0.000	0.001	0.000	0.000	0.001	0.000	0.000	0.000	0.000	0.000
Sb	0.000	0.000	0.000	0.000	0.000	0.000	0.000	0.000	0.000	0.000	0.000	0.000
Ni	0.595	0.599	0.599	0.601	0.596	0.597	0.594	0.595	0.594	0.589	0.596	0.598
Te	0.003	0.003	0.004	0.003	0.003	0.003	0.003	0.003	0.003	0.003	0.003	0.003

R = heazlewoodite in chromitite; L = heazlewoodite in chloritite; bdl = below detection limit.

temperature (>300 °C) prograde alteration during which developed Fe-rich chromite rims. Such Fe-rich chromite was also reported in the Shetland ophiolitic mélange. The Fe-rich chromite rims around the chrome-spinels to the east of Cliff preserve lower Fe^{3+} contents indicating a lower, predominantly greenschist metamorphic grade, and the Fe-rich chromite at Cliff chromitite with the highest Fe^{3+} content was interpreted as recording post-serpentinization Fe-rich chromite formation under relatively oxidizing conditions (Derbyshire et al., 2013). The Fe^{3+}/Fe^{2+} ratios of the studied Fe-rich chromite are highly variable and are mostly lower than that for chrome-spinel

Table 6
Representative compositions of maucherite in chromitite and in chloritite from Sartohay.

wt.%	R	R	R	R	R	R	R	R	R	L	L	L	L	L	L
Fe	0.25	0.35	0.48	0.57	0.24	0.32	0.02	0.33	0.51	0.56	0.04	0.30	0.24	0.51	0.44
As	45.84	45.83	46.86	45.29	45.21	45.21	45.22	45.21	45.71	45.09	45.29	45.14	45.49	45.63	46.01
S	0.24	0.67	0.34	0.37	0.36	0.32	0.32	0.36	0.29	0.38	0.31	0.36	0.22	0.61	0.34
Co	bdl	0.27	0.31	0.31	0.29	0.33	0.27	0.31	0.09	0.37	0.26	0.35	0.04	0.17	0.32
Sb	0.43	0.01	0.06	0.79	0.94	1.01	1.01	0.91	0.41	1.47	1.14	1.28	0.92	0.02	0.44
Ni	52.4	51.97	51.71	51.92	52.04	52.01	52.31	52.04	52.24	51.02	52.34	52.26	52.34	52.01	51.91
Te	0.70	0.73	0.53	0.67	0.91	0.64	0.79	0.79	0.71	0.66	0.69	0.74	0.73	0.79	0.54
Total	99.86	99.83	100.29	99.92	99.99	99.84	99.94	99.95	99.96	99.55	100.07	100.43	99.98	99.74	100.00
Atom															
Fe	0.003	0.004	0.006	0.007	0.003	0.004	0.000	0.004	0.006	0.007	0.000	0.004	0.003	0.006	0.005
As	0.401	0.399	0.407	0.396	0.396	0.396	0.396	0.395	0.399	0.397	0.396	0.393	0.398	0.397	0.401
S	0.005	0.014	0.007	0.008	0.007	0.007	0.007	0.007	0.006	0.008	0.006	0.007	0.005	0.010	0.007
Co	0.000	0.003	0.003	0.003	0.003	0.004	0.003	0.003	0.001	0.004	0.003	0.004	0.000	0.002	0.004
Sb	0.002	0.000	0.000	0.004	0.005	0.005	0.005	0.005	0.002	0.008	0.006	0.007	0.005	0.000	0.002
Ni	0.585	0.577	0.574	0.579	0.581	0.581	0.585	0.581	0.582	0.573	0.584	0.581	0.585	0.578	0.578
Te	0.004	0.004	0.003	0.003	0.005	0.003	0.004	0.004	0.004	0.003	0.004	0.004	0.004	0.004	0.003

R = maucherite in chromitite; L = maucherite in chloritite; bdl = below detection limit.
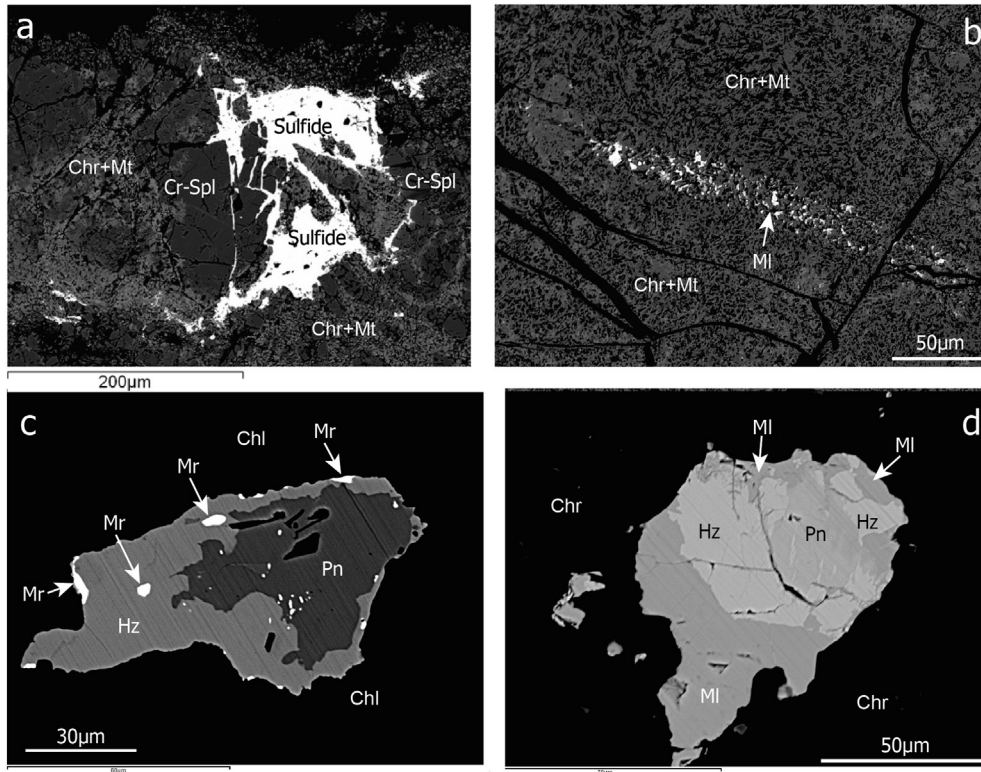
Fig. 6. BSE images showing Fe–Ni–As–S mineral assemblages in the Sartohay chromitite: (a) interstitial sulfide grains occurring among chrome-spinel grains, Fe-rich chromite, and magnetite; (b) millerite grains in Fe-rich chromite–magnetite assemblage; (c) heazlewoodite–maucherite assemblage replaced pentlandite; (d) pentlandite was replaced by heazlewoodite and millerite. For mineral abbreviations see Table 1.
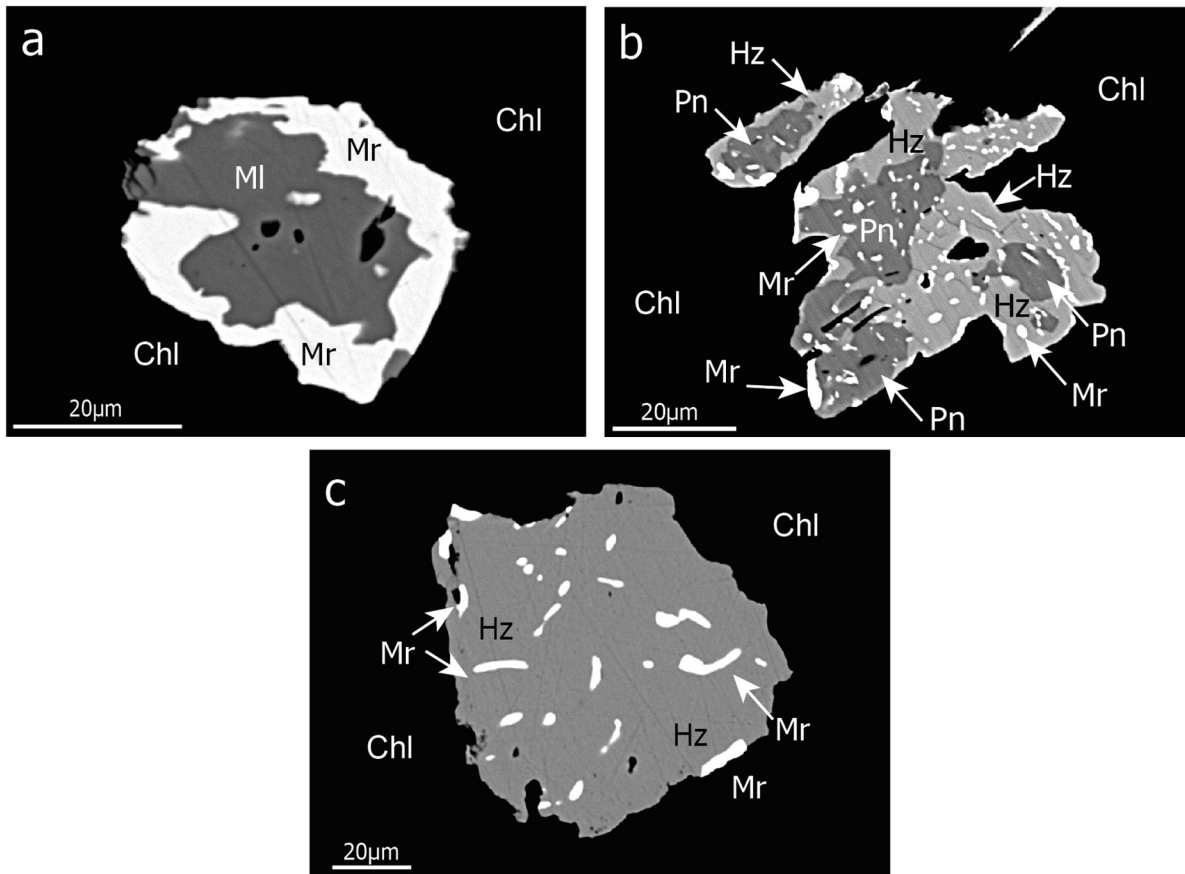
Fig. 7. BSE images showing two forms of maucherite: (a) maucherites replaced millerite; (b–c) worm-like maucherite in pentlandite and heazlewoodite. Chl — chlorite, for other mineral abbreviations see Table 1.
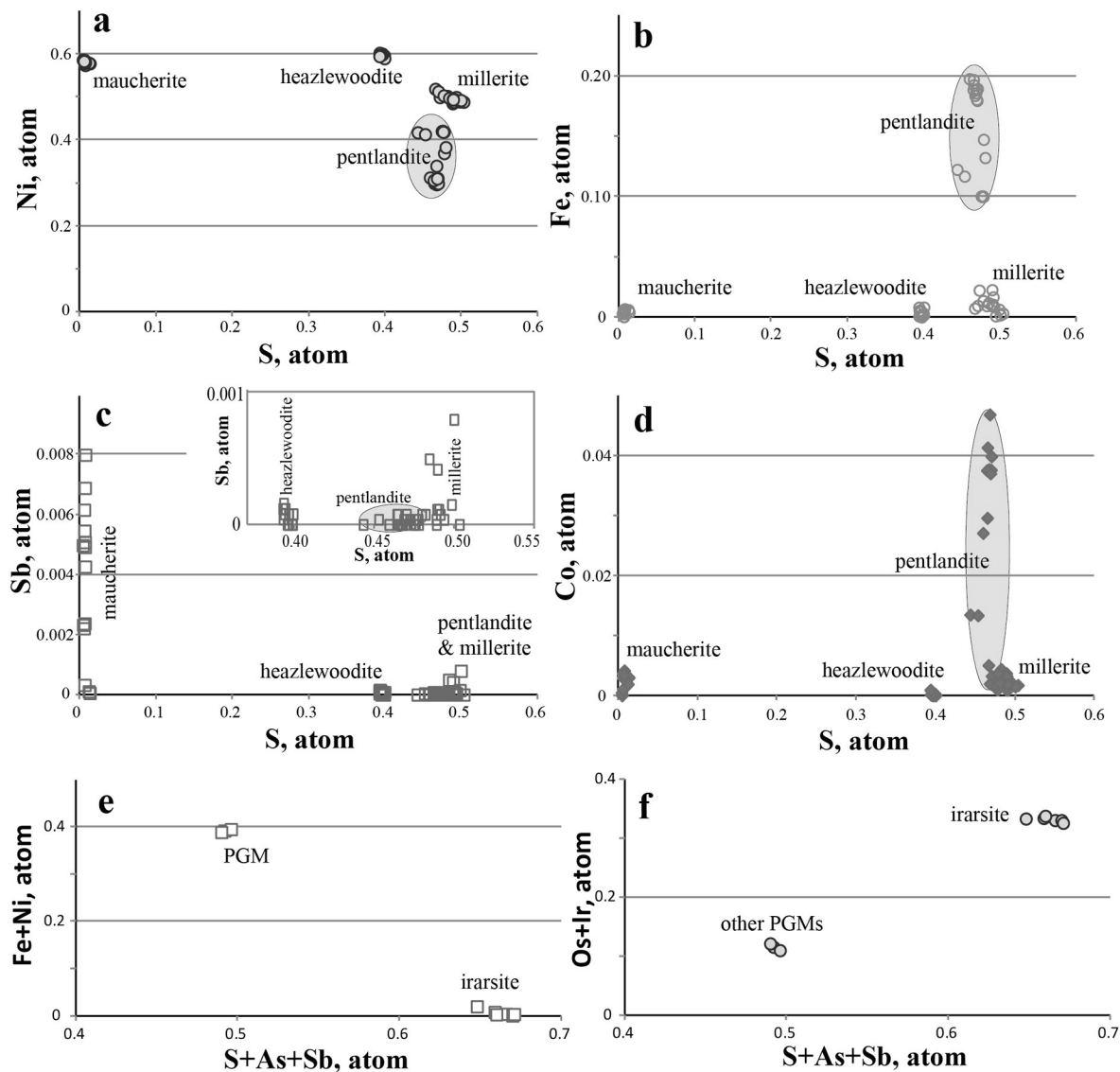
Fig. 8. (a–d) S vs. Ni, Fe, Sb, and Co contents for the studied Fe–Ni–As–S minerals; (e–f) Plots of S + As + Sb vs. Fe + Ni (e) and Os + Ir (f) showing the difference between irarsite and other PGMs.

cores (Table 2). In the Sartohay chromitite, the chrome-spinel was firstly altered to the above-described Fe-rich chromite, and further alteration transformed such Fe-rich chromite into magnetite (Figs. 3g, 4). These observations suggested a two-stage metasomatic process: one corresponding to the formation of the Fe-rich chromite at low-temperature with low fO_2 condition, while the following oxidizing metasomatic stage produced magnetite. Oxidized chrome-spinel displays significant non-stoichiometry due to the conversion of Fe^{2+} to Fe^{3+}, which results in lattice vacancies (Quintiliani et al., 2006). The substitution of Fe^{3+} for Fe^{2+} is rapid under post-serpentinization oxidation (Kimball, 1990). The mineral chemistry for the Sartohay chrome-spinels extend the Fe^{3+}/Fe^{2+} range to variable values (0.14–0.34, Table 2) compared to the chromitite and chrome-spinel from other localities with Fe^{3+}/Fe^{2+} ratios of 0.1–0.4 (Derbyshire et al., 2013).

5.2. Sulfides, arsenides, and PGMs: low-temperature hydrothermal origin

Sulfides, arsenides, and PGMs were observed mostly in the Fe-rich chromite, magnetite, and chloritite surrounding the chrome-spinel porphyroblasts in the Sartohay ophiolitic mélange. This and the fact that none of such minerals have been found occurring as inclusions

in chrome-spinel suggest their secondary origin. Crystallization of these minerals must be associated with hydrothermal process. Millerite mostly represents a low-temperature sulfide (Vaughan and Craig, 1978) that formed as a replacement of nickel-bearing sulfides (e.g., pentlandite, pyrrhotite). Fig. 11a shows the relationships among the observed sulfide minerals in the Sartohay chromitite. Both millerite and heazlewoodite analyses are very close to their end-members, while pentlandite has a much large compositional space in the Fe–S–Ni plot. All these sulfides also fill in the compositional spaces of sulfides formed in the Mount Keith (Yilgarn Craton, Western Australia) serpentinite during hydrothermal alteration. Disseminated Ni–Fe sulfide ore at Mount Keith range from least-altered assemblages of pentlandite–pyrrhotite–chalcopyrite to altered assemblages of pentlandite–heazlewoodite–millerite, and heazlewoodite (Gole, 2014). The coexistence of pentlandite and heazlewoodite has been attributed to the establishment of highly reducing conditions under low water/rock ratios and low temperatures (Klein et al., 2009). Petrographic observations suggest a systematic change from magnetite–pentlandite, pentlandite–heazlewoodite–maucherite, millerite–breithauptite, to millerite–godlevskite-PGMs-dominated assemblage in the Sartohay chromitites (Fig. 11b).
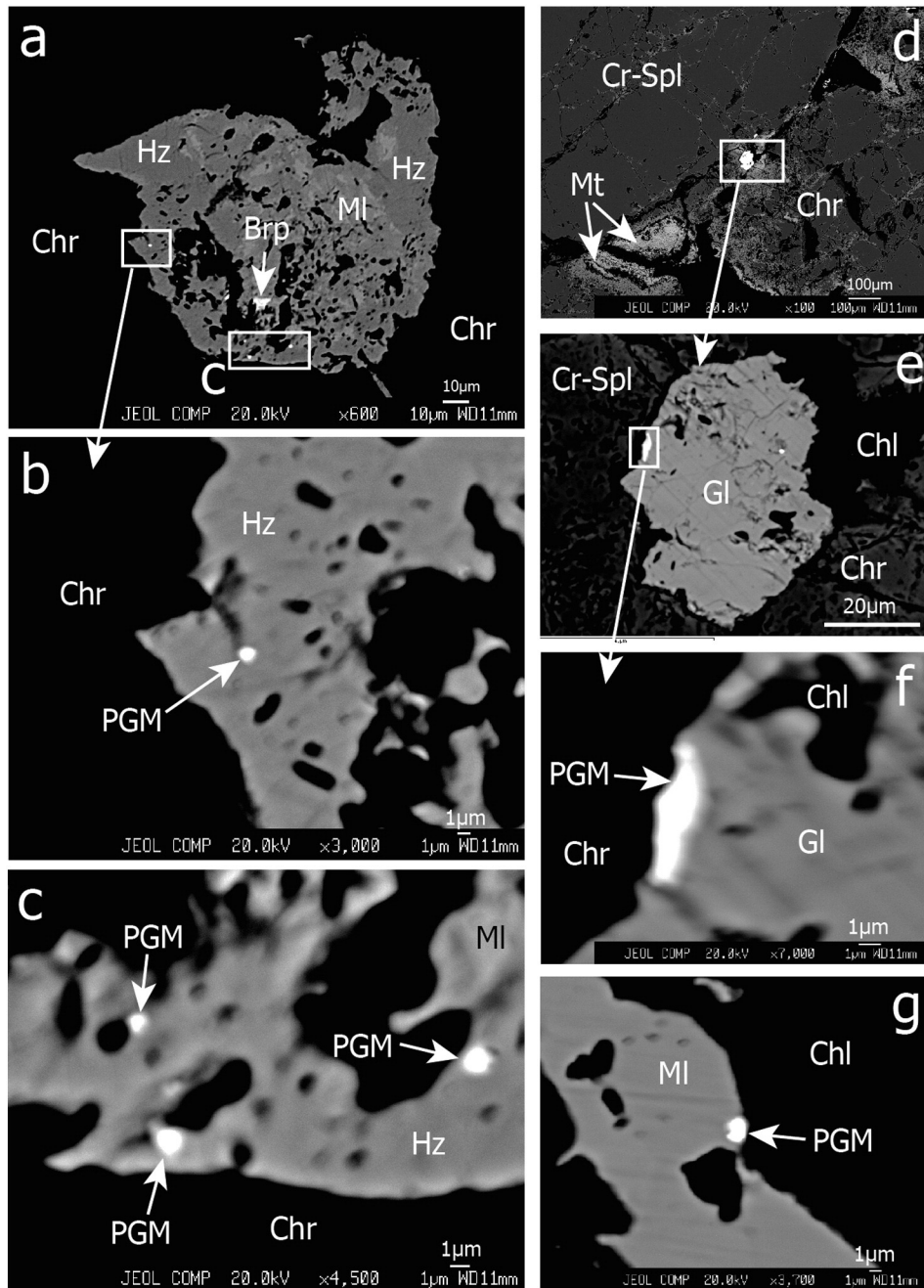
Fig. 9. BSE images showing PGMs in the Sartohay chromitite: (a–c) heazlewoodite replaced millerite with PGMs attached to its edge; (d–f) PGMs attached to godlevskite in the boundary of chrome-spinel; (g) a PGM grain occurring on the edge of millerite contacting with chlorite (Chl). For mineral abbreviations see Table 1.

All sulfides in the Sartohay chromitites are secondary that cannot control the distribution of PGE, and IPGEs probably were fractionated by irarsite as this mineral is the most common PGMs found in the Sartohay chromitites. PGEs are chalcophile elements and should fractionate into a sulfide phase owing to their large partition coefficient into the sulfide phase (Mungall and Brenan, 2014). Zhou et al. (2001) suggested that strong fractionation of PGE has taken place in the Sartohay chromitite, in which the abundance of Ir and Ru can reach 4 to 6 times higher, and Pd 10% lower than primitive mantle values. The Al-rich chromitite in the Sartohay deposit is thought to have formed by reaction between depleted harzburgite and upwelling MORB-type magma, and that the system reached S-saturation before the formation of chromitite. Consistent with our observations, this indicates that the parent magma of the Sartohay deposit had low concentrations of PGE and was especially depleted in Pd and Pt.

The enrichments of PGEs, Ni, Co, Sb, Te, and As in disseminated millerite, heazlewoods, maucherite, and irarsite reflect element mobility during hydrothermal process. Disseminated sulfides are depleted in PGEs due to late sulfide saturation and the PGE-depleted nature of the mantle source rocks. This is similar to serpentinized samples from the Bacuri complex in Amapa of northeastern Brazil (Prichard et al., 2001), in which the PGE were concentrated in chromitite and sulfide-bearing serpentinite, where pentlandite partially altered to millerite, maucherite and gersdorffite. The Os, Ir, and Ru concentrations in the chromitite are attributed to the presence of irarsite.

In summary, all the Fe–Ni–As–S minerals (sulfides, arsenides), breithauptite, magnetite, and PGMs are secondary mineral phases relative to chrome-spinel in the Sartohay chromitite. Their forming sequences shown in Fig. 11b are also illustrated in Fig. 11c. At first, chrome-spinel was transformed to the Fe-rich chromite probably
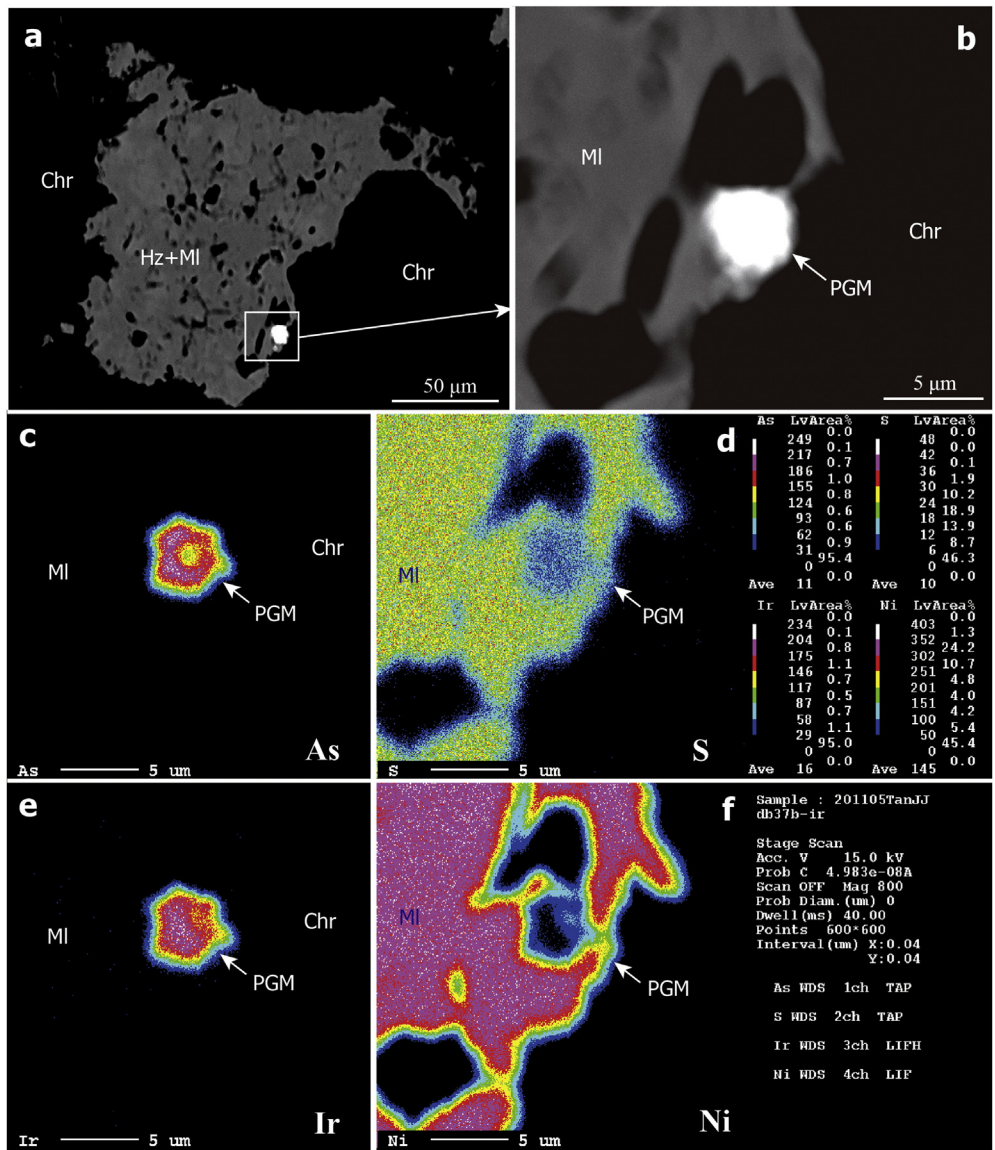
Fig. 10. (a–b) BSE images showing PGM grain in millerite; (c–f) X-ray mapping for PGM in the Sartohay chromitite.

Table 7
Representative compositions of platinum group mineral (PGM) in Sartohay chromitite.

wt.%	Irarsite	Irarsite	Irarsite	Irarsite	Irarsite	Irarsite	M-1	M-2	M-3
Os	4.94	5.49	7.28	4.99	2.42	1.84	11.32	10.76	26.24
Ir	56.68	57.22	54.99	58.76	60.02	61.19	21.91	18.08	3.43
Ru	1.18	0.27	0.64	0.02	0.21	0.02	0.12	2.12	3.02
Rh	0.03	0.21	bdl	bdl	0.01	bdl	bdl	bdl	0.68
Fe	0.11	0.21	0.17	0.01	0.01	0.08	0.11	0.51	1.32
As	24.38	24.37	23.42	24.22	24.21	24.82	0.27	0.92	0.02
S	10.77	10.16	10.19	10.21	10.41	10.91	21.19	22.11	23.04
Sb	1.29	1.47	1.69	1.06	2.02	0.69	9.91	9.03	7.27
Ni	0.12	0.24	0.97	0.15	0.01	0.12	34.72	35.74	34.82
Total	99.50	99.64	99.35	99.42	99.32	99.67	99.55	99.27	99.84
Atom									
Os	0.026	0.029	0.038	0.027	0.013	0.010	0.039	0.036	0.087
Ir	0.292	0.300	0.288	0.310	0.315	0.316	0.075	0.060	0.011
Ru	0.012	0.003	0.006	0.000	0.002	0.000	0.001	0.013	0.019
Rh	0.000	0.002	0.000	0.000	0.000	0.000	0.000	0.000	0.004
Fe	0.002	0.004	0.003	0.000	0.000	0.000	0.001	0.006	0.015
As	0.323	0.327	0.314	0.328	0.326	0.328	0.002	0.008	0.000
S	0.333	0.319	0.320	0.323	0.327	0.337	0.437	0.440	0.453
Sb	0.011	0.012	0.014	0.009	0.017	0.006	0.054	0.047	0.038
Ni	0.002	0.004	0.017	0.003	0.000	0.002	0.391	0.389	0.374

bdl = below detection limit.
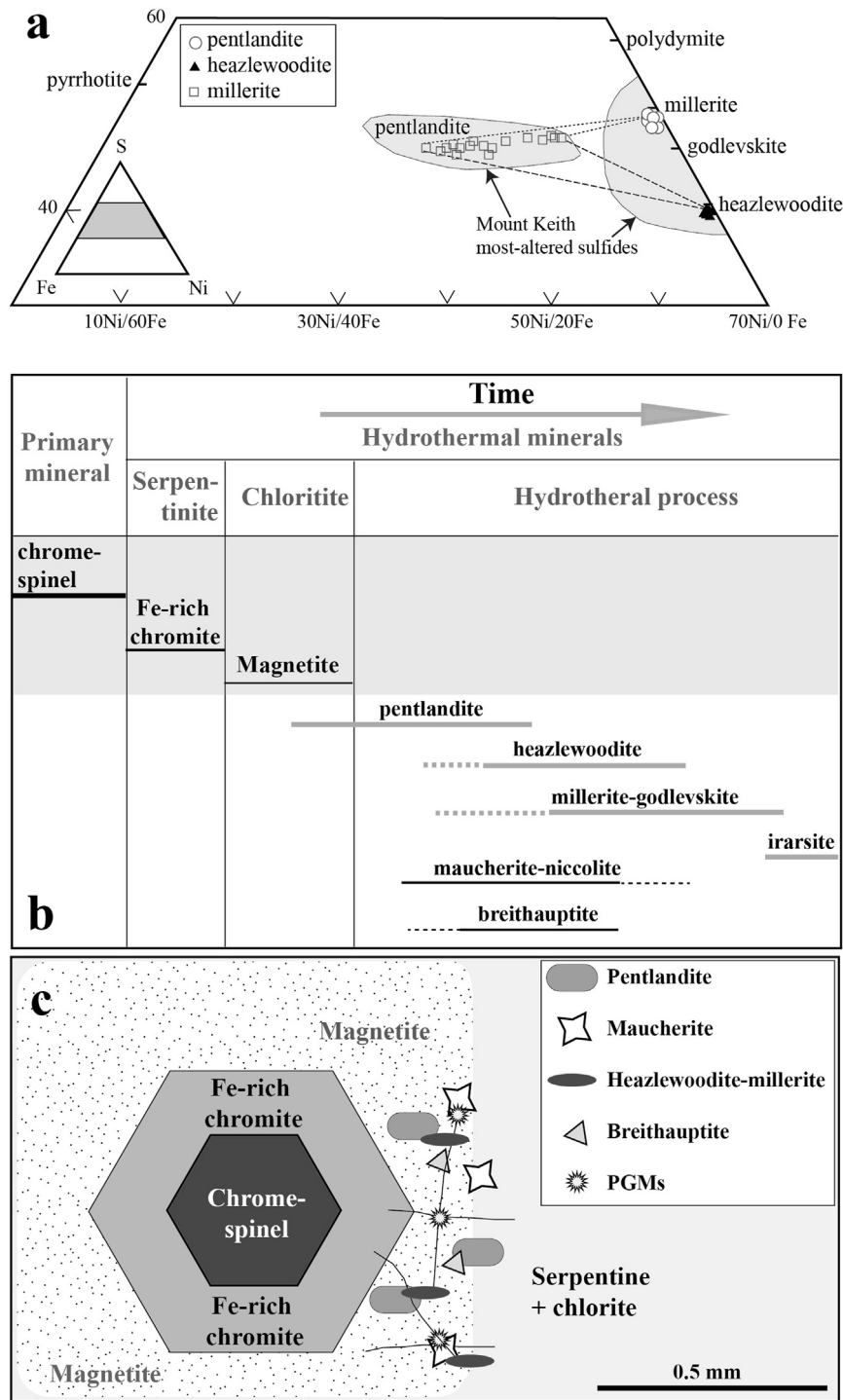
Fig. 11. (a) Triangular compositional diagrams for Fe–Ni–S minerals from the Sartohay chromitite (modified from Vaughan and Craig, 1978), sulfides from Mount Keith of Western Australia (Gole, 2014) are shown for comparison; (b) Sequence of minerals formed during serpentinization and following hydrothermal process in the Sartohay chromitites; (c) Model showing mineral phases generated during serpentinization and following hydrothermal processes.

during serpentinization at reduced condition. The Fe-rich chromite was altered to magnetite at relatively oxidizing condition, which probably happened during the formation of chloritite envelope surrounding chromitite. The following hydrothermal alteration introduced S, Sb, and Ni, which replaced magnetite and formed pentlandite, breithauptite, maucherite, and other sulfides. Millerite, heazlewoodite, and godlevskite generally replaced pentlandite. The irarsite formed at the final stage of hydrothermal processes with introduction of As, Ir, and Os.

6. Conclusions

A two-stage metasomatic process is recognized in the Sartohay chromitites: one corresponding to the formation of the Fe-rich chromite at low-temperature with low fO_2 condition, while the following oxidizing metasomatic stage produced magnetite. Afterwards, the Fe–Ni–As–S mineral assemblages, breithauptite, irarsite, and possibly other PGMs formed in the Sartohay chromitites. All these minerals are secondary origin relative to the chromitites and formed during hydrothermal

alteration overprinting the Sartohay chromitites. Micro-sized PGMs (irarsite in most cases) generally occur on the edges of millerite, heazlewoodite, and godlevskite. The documented systematic change from magnetite–pentlandite, pentlandite–heazlewoodite–maucherite, millerite–breithauptite, to millerite–godlevskite–irarsite-dominated assemblage suggested a complex evolutionary path in the $P–T–fS_2–fO_2$ space. The coexistence of pentlandite and heazlewoodite suggests a highly reducing condition at low temperature. The IPGEs probably were fractionated by irarsite as this mineral is the most common PGMs found in the Sartohay chromitites. The enrichments of Os, Ir, Sb, and As in disseminated millerite, breithauptite, heazlewoods, maucherite, and irarsite occurring within chromitites, indicate the mobility of Os, Ir, Sb, and As during low-temperature hydrothermal processes following serpentinization in the Sartohay ophiolitic mélange.

Conflict of interest

I declare that the paper "Platinum group mineral (PGM) and Fe–Ni–As–S minerals in the Sartohay chromitite, Xinjiang of China: implications for the mobility of Os, Ir, Sb, and As during hydrothermal processes" by Yongfeng Zhu, Juanjuan Tan, and Tian Qiu submitted to Ore Geology Reviews does not have any conflict of interests.

Acknowledgments

References

Ahmed, A.H., Arai, S., Ikenne, M., 2009. Mineralogy and paragenesis of the Co-Ni arsenide ores of Bou Azzer, Anti-Atlas, Morocco. Econ. Geol. 104, 249–266.

Auge, T., Genna, A., Legendre, O., Ivanov, K.S., Yuri, A.V., 2005. Primary platinum mineralization in the Nizhny Tagil and Kachkanar ultramafic complexes, Ural, Russia: a genetic model for PGE concentration in chromite-rich zones. Econ. Geol. 100, 707–732.

Brough, C.P., Prichard, H.M., Neary, C.R., Fisher, P.C., McDonald, I., 2015. Geochemical variations within podiform chromitite deposits in the Shetland ophiolite: implications for petrogenesis and PGE concentration. Econ. Geol. 110, 187–208.

Chen, B., Zhu, Y.F., 2008. Petrology of ultramafic rock in Darbut ophiolite (Xinjiang), evidence from Cr-spinel. Earth Sci. Front. 15, 312–322 (in Chinese with English abstract).

Chen, B., Zhu, Y.F., 2011. Petrology, geochemistry and zircon U–Pb chronology of gabbro in Darbut ophiolitic melange, Xinjiang. Acta Petrol. Sin. 27, 1746–1758 (in Chinese with English Abstract).

Derbyshire, E.J., O'Driscoll, B., Lenaz, D., Gertisser, R., Kronz, A., 2013. Compositionally heterogeneous podiform chromitite in the Shetland ophiolite complex (Scotland): implications for chromitite petrogenesis and late-stage alteration in the upper mantle portion of a supra-subduction zone ophiolite. Lithos 162–163, 279–300.

Evans, B.W., 2004. The serpentinite multisystem revisited: chrysotile is metastable. Int. Geol. Rev. 46, 479–506.

Feng, Y.M., 1986. Genetic environments and original types of ophiolites in west Junggar. Bull. Xi'an Inst. Geol. Min. Res., Chinese Acad. Geol. Sci. 13, 37–45 (in Chinese).

Finnigan, C.S., Brenan, J.M., Mungall, J.E., McDonough, W.F., 2008. Experiments and models bearing on the role of chromite as a collector of platinum-group minerals by local reduction. J. Petrol. 49, 1647–1665.

Foustoukos, D.I., Bizimis, M., Frisby, C., Shirey, S.B., 2015. Redox controls on Ni–Fe–PGE mineralization and Re/Os fractionation during serpentinization of abyssal peridotite. Geochim. Cosmochim. Acta 150, 11–25.

Gervilla, F., Padron-Navarta, J.A., Kerestedjian, T., 2012. Formation of ferrian chromite in podiform chromitites from the Golyamo Kamenyane serpentinite, Eastern Rhodopes, SE Bulgaria: a two-stage process. Contrib. Mineral. Petrol. 164, 643–657.

Gole, M.J., 2014. Leaching of S, Cu, and Fe from disseminated Ni–(Fe)–(Cu) sulphide ore during serpentinization of dunite host rocks at Mount Keith, Agnew–Wiluna belt, Western Australia. Mineral. Deposita 49, 821–842.

Grieco, G., Diella, V., Chaplygina, N.L., Savelieva, G.N., 2007. Platinum group elements zoning and mineralogy of chromitites from the cumulate sequence of the Nurali massif (Southern Urals, Russia). Ore Geol. Rev. 30, 257–276.

Gu, P.-Y., Li, Y., Zhang, B., Tong, L., Wang, J., 2009. LA–ICP-MS zircon U–Pb dating of gabbro in the Darbut ophiolite, western Junggar, China. Acta Petrol. Sin. 25, 1364–1372 (in Chinese with English abstract).

Junge, M., Wirth, R., Oberthür, T., Melcher, F., Schreiber, A., 2015. Mineralogical sitting of platinum-group elements in pentlandite from the Bushveld complex, South Africa. Mineral. Deposita 50, 41–54.

Kapsiotis, A., Grammatikopoulos, T.A., Tsikouras, B., Hatzipanagiotou, K., Zaccarini, F., Garuti, G., 2011. Mineralogy, composition and PGM of chromites from Pefki, Pindos ophiolite complex (NW Greece): evidence for progressively elevated fAs conditions in the upper mantle sequence. Mineral. Petrol. 101, 129–150.

Kimball, K., 1990. Effects of hydrothermal alteration on the composition of chromian spinels. Contrib. Mineral. Petrol. 105, 337–346.

Klein, F., Bach, W., Jons, N., McCollom, T., Moskowitz, B., Berquo, T., 2009. Iron partitioning and hydrogen generation during serpentinization of abyssal peridotites from 15°N on the Mid-Atlantic Ridge. Geochim. Cosmochim. Acta 73, 6868–6893.

Liu, X.-J., Xu, J.-F., Wang, Q.-S., Hou, Y.-Q., Bai, Z.-H., Lei, M., 2008. Geochemistry of dating of E-MORB type mafic rocks from Dalabute ophiolite in west Junggar, Xinjiang and geological implications. Acta Petrol. Sin. 25, 1373–1389 (in Chinese with English abstract).

McGowan, N.M., Griffin, W.L., González-Jiménez, J.M., Belousova, E., Afonso, J.C., Shi, R., McCammon, C.A., Pearson, N.J., O'Reilly, S.Y., 2015. Tibetan chromitites: excavating the slab graveyard. Geology 43, 179–182.

Mellini, M., Rumori, C., Viti, C., 2005. Hydrothermally reset magmatic spinels in retrograde serpentinites: formation of 'ferritchromit' rims and chlorite aureoles. Contrib. Mineral. Petrol. 149, 266–275.

Merlini, A., Grieco, G., Diella, V., 2009. Ferritchromit and chromium-chlorite formation in melange-hosted Kalkan chromitite (Southern Urals, Russia). Am. Miner. 94, 1459–1467.

Mungall, J.E., Brenan, J.M., 2014. Partitioning of platinum-group elements and Au between sulfide liquid and basalt and the origins of mantle–crust fractionation of the chalcophile elements. Geochim. Cosmochim. Acta 125, 265–289.

Prichard, H.M., Sa, J.H.S., Fisher, P.C., 2001. Platinum-group mineral assemblages and chromite composition in the altered and deformed Bacuri complex, Amapa, northeastern Brazil. Can. Mineral. 39, 377–396.

Qiu, T., Zhu, Y.-F., 2015. Geology and geochemistry of listwaenite-related gold mineralization in the Sayi gold deposit, Xinjiang, NW China. Ore Geol. Rev. 70, 61–79.

Quintiliani, M., Andreozzi, G.B., Graziani, G., 2006. Fe^{2+} and Fe^{3+} quantification by different approaches and fO_2 estimation for Albanian Cr-spinels. Am. Miner. 91, 907–916.

Robinson, P.T., Trumbull, R.B., Schmitt, A., et al., 2015. The origin and significance of crustal minerals in ophiolitic chromitites and peridotites. Gondwana Res. 27, 486–506.

Uysal, I., Tarkian, M., Sadiklar, M.B., Zaccarini, F., Meisel, T., Garuti, G., Heidrich, S., 2009. Petrology of Al- and Cr-rich ophiolitic chromitites from the Mugla, SW Turkey: implications from composition of chromite, solid inclusions of platinum-group minerals, silicate and base-metal minerals and Os-isotope geochemistry. Contrib. Mineral. Petrol. 158, 659–674.

Vaughan, D.J., Craig, J.R., 1978. Mineral Chemistry of Metal Sulfides. Cambridge University Press, London (493 pp.).

Yang, J.-S., Dobrzhinetskaya, L., Bai, W.J., 2007. Diamond- and coesite-bearing chromitites from the Luobusa ophiolite, Tibet. Geology 35, 875–878.

Yang, J.-S., Meng, F.-C., Xu, X.Z., Robinson, P.T., Dilek, Y., Makeyev, A.B., Wirth, R., Wiedenbeck, M., Cliff, J., 2015. Diamonds, native elements and metal alloys from chromitites of the Ray-Iz ophiolite of the Polar Urals. Gondwana Res. 27, 459–485.

Zhou, M.-F., Robinson, P.T., Malpas, J., Aitchison, J., Sun, M., Bai, W., Hu, X., Yang, J., 2001. Melt/mantle interaction and melt evolution in the Sartohay high-Al chromite deposits of the Dalabute ophiolite (NW China). J. Asian Earth Sci. 19, 517–534.

Zhou, M.-F., Robinson, P.-T., Su, B.-X., Gao, J.-F., Li, J.-W., Yang, J.-S., Malpas, J., 2014. Compositions of chromite, associated minerals, and parental magmas of podiform chromite deposits: the role of slab contamination of asthenospheric melts in suprasubduction zone environments. Gondwana Res. 26, 262–283.

Zhu, Y.-F., 2008. K- and Si-rich glasses in harzburgite from Damaping, north China. Island Arc 17, 560–576.

Zhu, Y.-F., 2011. Zircon U–Pb and muscovite $^{40}Ar/^{39}Ar$ geochronology of the gold-bearing Tianger mylonitized granite, granite, Xinjiang, northwest China: implications for radiometric dating of mylonitized magmatic rocks. Ore Geol. Rev. 40, 108–121.

Zhu, Y.-F., Xu, X., 2006. The discovery of early Ordovician ophiolite mélange in Taerbahatai Mts., Xinjiang, NW China. Acta Petrol. Sin. 22, 2823–2842 (in Chinese with English abstract).

Zhu, Y.-F., Chen, B., Xu, X., Qiu, T., An, F., 2013. A new geological map of the western Junggar, north Xinjiang (NW China): implications for Paleoenvironmental reconstruction. Episodes 36, 205–220.

Zhu, Y.-F., Chen, B., Qiu, T., 2015. Geology and geochemistry of the Baijiantan–Baikouquan ophiolitic mélanges: implications for geological evolution of west Junggar, Xinjiang, NW China. Geol. Mag. 152, 41–69.

Zhu, Y.-F., Qiu, T., Li, X.-H., 2015n. SIMS U–Pb Chronology of Metagabbros and Listwaenite in the Sartohay Chromitites, Constraints on the Ore-forming Time of Chromitites in Ophiolitic Mélange (in preparation).